Understanding the distribution of relaxation times of a low–Pt PEM fuel cell

Tatyana Reshetenko[1, a)] and Andrei Kulikovsky[2, b)]
[1)] *Hawaii Natural Energy Institute*
University of Hawaii
Honolulu, Hawaii 96822, USA
[2)] *Theory and Computation of Eenergy Materials (IEK-13)*
Institute of Energy and Climate Research
Forschungszentrum Jülich GmbH
D–52425 Jülich, Germany [c)]

(Dated: 18 July 2021)

Distribution of relaxation times (DRT) is calculated from fifty local impedance spectra of a low–Pt PEM fuel cell. 48 out of 50 DRT spectra contain three peaks. Evolution of the peak frequency positions and resistivities with the cell current density are analyzed. The analysis allows us to attribute the low–frequency peak to oxygen transport in the gas–diffusion layer (perhaps, including transport in the channel), the middle peak to unresolved processes of charge–transfer and oxygen transport in the ionomer film, and the high-frequency peak to oxygen transport in void pores of the catalyst layer. Comparison of DRT spectra of low–Pt and high–Pt cells suggests a novel method for measuring ionomer film transport resistivity in a low–Pt cell.

Keywords: PEMFC impedance, DRT, low–Pt loading

I. INTRODUCTION

At present, typical PEMFC–based 100-kW stack for automotive applications contains about 100 grams of precious metal providing high rate of the oxygen reduction reaction (ORR). Lowering of this parameter is of paramount importance for wide commercialization of PEM fuel cell technology. However, attempts to lower Pt content by a factor of three to four have revealed unexpected "overlinear" voltage loss of a PEM fuel cell[1,2]. This loss has been attributed to oxygen transport through a thin ionomer film covering Pt/C agglomerates in a cell cathode[2–7]. Qualitatively, as any other oxygen transport layer, ionomer film covering Pt/C agglomerates determines a limiting current density j_{lim}^N, which is proportional to the Pt loading. In a high–Pt cell, oxygen flux to a single Pt/C agglomerate is not large, the total O_2 flux expressed in electric units is far from j_{lim}^N, and the ionomer film practically does not affect the cell performance. However, in a low–Pt cell, the number of agglomerates per unit cell surface area is much lower, j_{lim}^N is three to four times less and the total oxygen flux in the electrode may reach j_{lim}^N, which seriously lowers the cell potential.

The effect of ionomer (typically Nafion) film has been studied experimentally using the limiting current method technique[5,7]. This technique is based on measuring the film transport resistivity in a cell operating close to the limiting current density, typically at low oxygen concentration, or even with hydrogen instead of oxygen[8]. A simple method for measuring film resistivity under real cell operating conditions would be highly desirable.

Electrochemical impedance spectroscopy (EIS) is a unique tool for fuel cells testing and characterization without interruption of current production mode. Analysis of impedance spectra can be performed either by spectra fitting using a relevant physics–based model, or by means of distribution of relaxation times (DRT) technique. Physics–based modeling is a complicated task requiring computing resources and time, while calculation of DRT is simple and fast procedure.

DRT function $\gamma(\tau)$ is a solution to equation[9–14]

$$Z(\omega) = R_\infty + R_{pol} \int_0^\infty \frac{\gamma(\tau)\, d\tau}{1 + \mathrm{i}\omega\tau} \tag{1}$$

where Z is the fuel cell impedance, ω is the angular frequency, R_∞ is the high–frequency cell resistance, and R_{pol} is the total polarization resistance of the cell given by total diameter of the Nyquist spectrum.

Impedance of a parallel RC–circuit is $R/(1 + \mathrm{i}\omega RC)$. Comparing this to Eq.(1), it became clear that Eq.(1) is expansion of cell impedance over infinite sum of parallel RC–circuit impedances, each one having the resistivity $R_{pol}\gamma\, d\tau$. From Eq.(1) it follows that the DRT spectrum of a single parallel RC–circuit is the Dirac δ–function positioned at $\tau_* = RC$.

[a)] Electronic mail: tatyanar@hawaii.edu
[b)] ISE member; Corresponding author; Electronic mail: A.Kulikovsky@fz-juelich.de
[c)] Also at:Lomonosov Moscow State University, Research Computing Center, 119991 Moscow, Russia

The cell impedance is usually measured at equidistant on log–scale frequencies $\{f_i, i = 1, \dots, N\}$, i.e., for $\ln(f_{i+1}) - \ln(f_i)$ independent of i (this is seen in Figure 2b). For numerical calculation of DRT it is thus beneficial to consider function $G(\tau)$, which obeys to equation

$$Z(\omega) = R_\infty + R_{pol} \int_{-\infty}^{\infty} \frac{G(\tau)\, d\ln(\tau)}{1 + \mathrm{i}\omega\tau} \tag{2}$$

Obviously, since $\tau = 1/(2\pi f)$,

$$\gamma(\tau) = \frac{G(\tau)}{\tau}, \quad \text{or} \quad G(f) = \frac{\gamma(f)}{2\pi f} \tag{3}$$

where f is the regular frequency (Hz). It follows that the dimension of γ is s^{-1}, while G is the dimensionless function. Setting in Eqs.(1), (2) $\omega = 0$ and taking into account that $Z(0) - R_\infty = R_{pol}$, we see that γ and G obey to the respective normalization conditions

$$\int_0^\infty \gamma(\tau)\, d\tau = 1, \quad \int_{-\infty}^{\infty} G(\tau)\, d\ln(\tau) = 1 \tag{4}$$

A great advantage of DRT spectra over standard impedance is that the functions γ and G are extremely sensitive to RC–like components in the impedance spectrum. All kinetic and transport processes in a fuel cell eventually are linked to charging/discharging of the double layer at the cathode catalyst/ionomer interface. One, therefore, may expect that the spectra of individual processes in the cell are close to RC–circuit spectrum. If, in addition, the resonance frequencies of individual processes are well separated on the frequency scale, the spectrum of $\gamma(f)$ and/or $G(f)$ consists of a number of well separated peaks. The peak frequency position f_n gives characteristic frequency of the process, and the area under each peak on the τ–scale gives the contribution R_n of this process to the total R_{pol}:

$$R_n = R_{pol} \int_{\tau_n}^{\tau_{n+1}} \gamma(\tau)\, d\tau = R_{pol} \int_{\tau_n}^{\tau_{n+1}} G(\tau)\, d\ln(\tau) \tag{5}$$

where τ_n, τ_{n+1} are peak boundaries.

Analysis of DRT spectra of solid oxide fuel cells is a well–established field (see a review[15]), while in studies of low–temperature PEM fuel cells, DRT is a relatively new technique[14]. DRT analysis of high–temperature PEM fuel cell has been performed in[16]. Due to the absence of liquid water in the cell, SOFC and HT-PEMFC impedance spectra are remarkably smooth. DRT analysis of "noisy" low–temperature PEMFC spectra is more difficult task. DRT of standard, high–Pt cells have been analyzed in[14,17]. To the best of our knowledge, so far DRT spectra of low–Pt PEMFC have been considered just in[18].

Eqs.(1),(2) belong to the class of Fredholm equations of the first kind. Direct numerical approximation of Eqs.(1),(2) leads to an ill–posed problem and numerical methods for solution of Eqs.(1), (2) are usually based on variants of Tikhonov's regularization technique[12,19–21] (see also review[22]). In this work, Eq.(2) is solved numerically using our most recent scheme based on non–negative least squares (NNLS)[23] solution of the Tikhonov's regularized system of equations[24]. This approach allows us to avoid projected gradient iterations suggested in[24], as NNLS method does this job much faster. The Python code "DRT_Gfun_nnls_*.zip" for calculation of DRT $G(f)$ from fuel cell impedance can be downloaded from https://github.com/akulikovsky/DRT-python-code. The symbol * in the file name substitutes the version number; currently 1.0.

II. IMPEDANCE AND DRT OF A LOW–PT CELL

Local impedance spectra of a low–Pt PEM fuel cell have been measured using the segmented cell setup (Figure 1). Due to continuous depletion of oxygen along the flow field, localized accumulation of water and buildup of impurities, spatial inhomogeneities may exist in the fuel cell resulting in local effects over the cell active area[25,26]. For the sake of comparison, local spectra of a standard, high–Pt cell have also been measured. Two cells with the cathode Pt loading of 0.1 mg$_{Pt}$ cm^{-2} and 0.4 mg$_{Pt}$ cm^{-2}, and active area of 76 cm^2 have been equipped with the flow field and gas–diffusion media separated into ten electrically insulated segments on the cathode side. The AC signal has been applied simultaneously to all the segments; the response has been measured from each segment and from the whole fuel cell. Impedance spectra processed in this work have been collected for the cell current density varying in the range 200 to 800 mA cm^{-2}. The cell parameters and operating conditions are listed in Table I; more experimental details can be found in[27,28].

Figure 2 shows example of the the whole low–Pt cell spectrum measured at the current density of 800 mA cm^{-2}. Figure 3

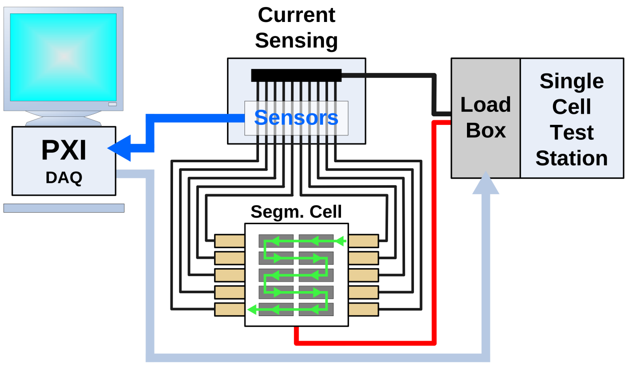

FIG. 1. The schematic of the segmented cell system[27]. The flowfield and GDL on the cathode side are separated into ten electrically insulated segments. The segmented cell setup allows us to measure impedance and local currents from individual segments and from the whole cell. More experimental details can be found in[27].

	Low-Pt	High-Pt
Catalyst loading A/C, mg cm^{-2}	0.1/0.1	0.4/0.4
CCL thickness l_t, μm	3.0	11.0
GDL thickness l_b, μm	230	
Air channel depth h, cm	0.1	
Flow stoichiometry A/C	2/4	
Relative humidity A/C	100%/50%	
Absolute pressure, A/C kPa	150/150	
Cell temperature, K	273 + 80	

TABLE I. Parameters and operating conditions of low–Pt and high–Pt cells. A/C stands for anode/cathode.

shows DRT of the impedance spectrum from the first segment of the low–Pt cell, calculated from the real part of Eq.(2) using the real part of experimental impedance. The optimal regularization parameter λ for Tikhonov's regularization has been calculated using the L–curve method[29]. In most of the variants,

The leftmost peak in Figure 3 can be attributed to oxygen transport in the gas–diffusion layer (GDL), or perhaps in the GDL and channel. The middle peak in Figure 3 represents two unresolved processes of oxygen transport in the ionomer film and charge transfer. The rightmost peak in Figure 3 manifests oxygen transport in void pores of the cathode catalyst layer (CCL). The remaining part of the paper provides arguments supporting these statements.

III. RESULTS AND DISCUSSION

The high–frequency part of impedance spectra (typically, above 2 kHz) contains the points with positive imaginary part. It this frequency range, fuel cell impedance is masked by the cable inductance, and the points with $\mathrm{Im}\,(Z) > 0$ have been discarded. Prior to DRT calculation, the real part of the remaining most high–frequency point has been subtracted from the cell impedance. This procedure eliminates R_∞ from Eq.(2) and the real part of this equation takes the form

$$Z_{re,*}(\omega) = R_{pol} \int_{-\infty}^{\infty} \frac{G(\tau)\, d\ln(\tau)}{1 + \omega^2\tau^2} \tag{6}$$

where $Z_{re,*} = Z_{re} - R_\infty$, and the subscript "re" denotes real part.

Calculated DRT of 48 out of 50 spectra acquired from ten segments of the low–Pt cell for the current densities of 200, 300, 400, 600 and 800 mA cm^{-1} consist of three peaks, quite similar to the spectra in Figure 3. The exclusion are two spectra from the 4th segment at the current densities of 200 and 300 mA cm^{-2} containing four peaks. The nature of the fourth peak at the frequency of about 1000 Hz is not clear and this peak has been ignored.

Processing of ten local DRT spectra for every current density allowed us to calculate mean over the segments peak frequency position, peak resistance, and the corresponding standard deviations. Let the peak characteristic frequencies

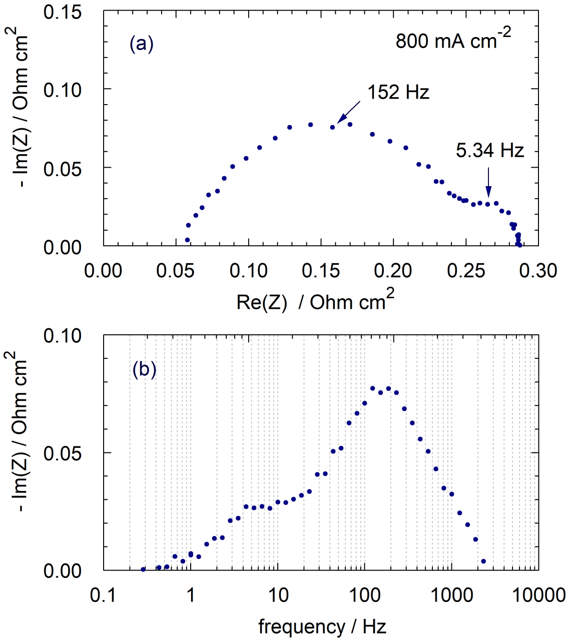

FIG. 2. (a) Experimental Nyquist spectrum of the low–Pt PEM fuel cell impedance at the cell current of 800 mA cm^{-2}. (b) Frequency dependence of the imaginary part of impedance in (a).

numbered in the ascending order be $\{f_n, n = 1, 2, 3\}$ (Figure 3a). Figure 4 shows the dependence of frequency positions of peaks 2 and 3 on the cell current density. Note quite small confidence intervals for the curve f_2 in Figure 4, meaning that the spread of f_2 between the segments is small. The frequencies of peak 3 (Figure 4) exhibit quite large statistical spread with no distinct dependence on segment number.

Position f_1 and resistivity R_1 of the first (leftmost) DRT peak exhibit distinct trends along the cathode channel: f_1 decreases while R_1 increases with the distance from the inlet (Figure 5). Assuming that the first peak represents oxygen transport in the GDL, we may expect that f_1 obeys to the Warburg finite–length formula

$$f_1 \simeq \frac{2.54 D_b}{2\pi l_b^2} \tag{7}$$

where D_b is the GDL oxygen diffusivity, and l_b is the GDL thickness. With l_b from Table I and f_1 decaying from 20 Hz at the channel inlet down to 2 Hz at the outlet (Figure 5a), we get quite realistic range of D_b variation from $2.6 \cdot 10^{-2}$ cm^2 s^{-1} at the inlet to $2.6 \cdot 10^{-3}$ cm^2 s^{-1} at the outlet. The decay of GDL oxygen diffusivity along the channel is accompanied by the growth of the GDL oxygen transport resistivity toward the outlet (Figure 5b). Strong decay of f_1 and the growth of the first peak resistivity along the cathode channel suggest higher liquid water content in the GDL of remote segments. With the growth of cell current density, the GDL water content becomes more uniform along the channel and the f_1–shape in Figure 5a becomes more flat. The growth of mean along the channel D_b with the cell current could be attributed to better water transport in the GDL at higher currents. The mechanism of this effect presumably is due to higher air flow velocity in the channel at higher currents, which facilitates liquid water removal from the GDL.

The first peak may also represent merged peaks of oxygen transport in the GDL and in the cathode channel. The characteristic frequency f_h of oxygen transport in channel is[30]

$$f_h = \frac{3.3 v}{2\pi L} \tag{8}$$

where v is the flow velocity and L is the channel length. The flow oxygen stoichiometry λ is given by

$$\lambda = \frac{4 F h v c^{in}}{L j_0} \tag{9}$$

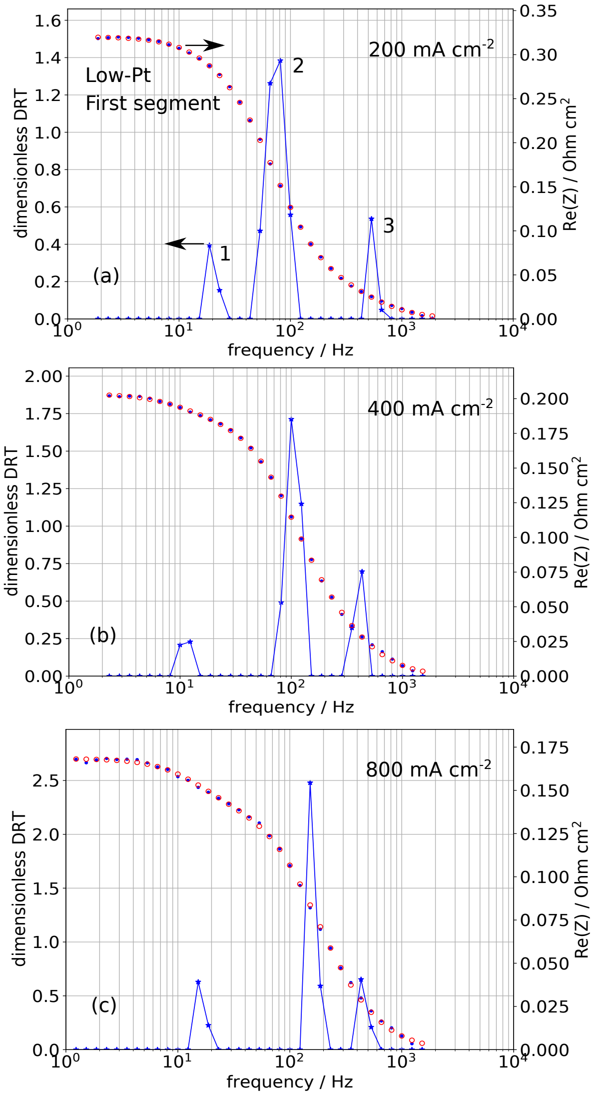

FIG. 3. DRT $G(f)$ of impedance spectra from the first segment of a low–Pt PEMFC (solid blue line and stars) calculated using Eq.(2) and the real part of impedance (blue dots). Red open circles show real part of impedance reconstructed from the calculated DRT using real part of Eq.(6).

where h is the channel depth. Combining (8) and (9), we get

$$f_h = \frac{0.825\lambda j_0}{2\pi F h c^{in}} \tag{10}$$

With the data from Table I, we get $f_h \simeq 2$ to 6 Hz, as j_0 increases from 0.2 to 0.8 A cm^{-2}. These values are close to the first peak frequency f_1 in the DRT spectra. We, thus, could assume that the first peak represents oxygen transport in a combined "GDL + channel" media. The growth of R_1 along the channel then correlates with the growth of the second, low–frequency arc in the local Nyquist spectra (Figure 6). This effect has first been demonstrated in experiments[31] and discussed in modeling studies[32–34]. Note that development of analytical model for the "GDL + channel" impedance is a field of ongoing research[35].

The growth of the second peak frequency f_2 with the cell current j_0 (Figure 4) is explained by growth of the frequency f_{ct} of faradaic (charge transfer) process, which presumably gives the main contribution to this peak. At low cell currents

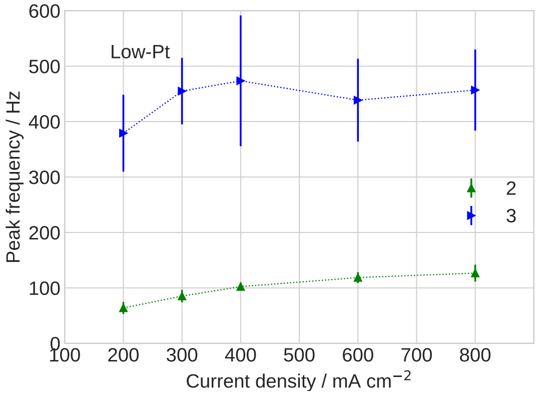

FIG. 4. Mean over ten segments frequency of DRT peaks 2 and 3 of the low–Pt cell vs cell current density. Peak numbering is shown in Figure 3a. The frequency position of the first peak strongly depends on coordinate along the channel (Figure 5a).

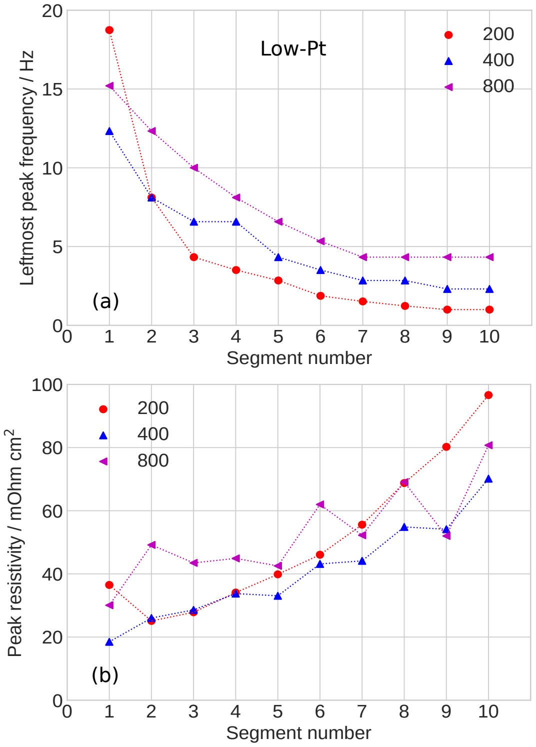

FIG. 5. (a) Frequency position and (b) resistivity of the first (leftmost) DRT peak of the low–Pt cell vs distance along the cathode channel for the indicated cell current densities (mA cm^{-2}).

f_{ct} is proportional to j_0, as the charge–transfer resistivity R_{ct} is inversely proportional to j_0[36]:

$$f_{ct} = \frac{1}{2\pi R_{ct} C_{dl} l_t} = \frac{j_0}{2\pi b C_{dl} l_t}, \quad R_{ct} = \frac{b}{j_0} \tag{11}$$

where C_{dl} is the double layer volumetric capacitance and b is the ORR Tafel slope. The average frequency position f_3 of the last, third peak is nearly independent of the cell current density (Figure 4).

To understand better the nature of the second and third peaks, we calculated DRT of local spectra of the high–Pt cell

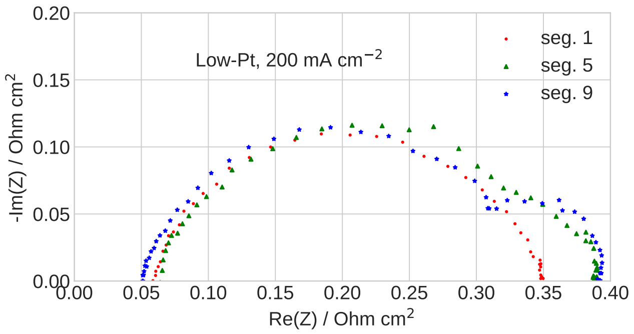

FIG. 6. Local impedance spectra of a low–Pt cell at the current density of 200 mA cm^{-2}. Note the growth of the low–frequency arc with the distance from the inlet.

with the standard cathode Pt loading of 0.4 mg$_{Pt}$ cm^{-2}. The spectra have been measured using the same segmented cell setup under the same operating conditions (Table I)[37]. Quite similar to the low–Pt cell, the local DRT spectra of the high–Pt cell exhibit three peaks (Figure 7). Figure 8 shows comparison of polarization resistivities of peaks 1 to 3 in the low–Pt and high–Pt cells. In the low–Pt cell, the second peak resistivity exhibits distinct decay with j_0, followed by flattening at higher currents (Figure 8). In the high–Pt cell, the resistivity of peak 2 also decreases with the cell current density, suggesting that peak 2 exhibits the faradaic process in the cell. However, the gap between the low–Pt and high–Pt peak 2 curves (shaded area in Figure 8) increases with the current. This indicates that in the low–Pt cell, peak 2 includes some additional resistivity, which increases with the cell current. Analysis shows that the characteristic frequencies of charge–transfer and oxygen transport in ionomer film differ by the factor of $\sqrt{3}$ (Ref.[38]), and the respective DRT peaks could merge in one. The peak 2 representing practically pure charge–transfer resistivity in a high–Pt cell decreases with the cell current, while significant contribution of ionomer–transport resistivity flattens the resistivity of peak 2 of the low–Pt cell at higher currents (Figure 8). We presume that both the low–Pt and high–Pt Gore cells employ the same Pt/C catalyst on the cathode side and hence in the absence of ionomer film resistivity, the two upper curves in Figure 8 should coincide. Thus, the shaded area in Figure 8 represents oxygen transport resistivity of ionomer film.

In the low–Pt and high–Pt cells, the resistivity of peak 3 weakly depends on cell current density (Figure 8). We assume that in both the cells, the high–frequency peak 3 represents oxygen transport in void pores. In[18], we attributed the third DRT peak of the low–Pt cell to oxygen transport in the void pores *and* ionomer film. However, weak dependencies of f_3 and of the 3rd peak resistivity on cell current suggest that f_3–peak represents oxygen transport in void pores only. Taking again for the estimate Warburg finite–length formula $f_3 \simeq 2.54 D_{ox}/(2\pi l_t^2)$, for the oxygen diffusivity in void pores of a low–Pt cell we get $D_{ox} \simeq 10^{-4}$ cm^2 s^{-1}. Here, $l_t = 3 \cdot 10^{-4}$ cm and $f_3 \simeq 450$ Hz (Figure 4). This value of D_{ox} agrees well with the value obtained from fitting the physics–based model to the local impedance spectra (to be published). From Figure 8 it follows that D_{ox} practically does not change with the cell current density in the range of 200 to 800 mA cm^{-2}. Note that reported in[28] growth of D_{ox} up to $6 \cdot 10^{-3}$ cm^2 s^{-1} at 800 mA cm^{-2} was based on fitting a single spectrum. Such a high D_{ox} is confirmed neither by the data from fitted local spectra, nor by the present results.

The value of $D_{ox} \simeq 10^{-4}$ cm^2 s^{-1} is an order of magnitude higher than the oxygen diffusivity in water, and at least an order of magnitude lower than the oxygen diffusion coefficient in a free void space of a dry catalyst layer[39]. $D_{ox} \simeq 10^{-4}$ cm^2 s^{-1} suggests that the void pores of a low–Pt cell are partially flooded, as predicted in[40]. Further, comparison of low–Pt and high–Pt resistivity curves for the third peak shows that in the low–Pt cell, the resistivity R_{ox} of oxygen transport in void pores is about 1.5 times higher than in the high–Pt cell (Figure 8). This resistivity is proportional to l_t/D_{ox}; for the estimates we take the low–current formula[41]

$$R_{ox} = \frac{b l_t}{12 F D_{ox} c_1} \tag{12}$$

where c_1 is the oxygen concentration at the CCL/GDL interface. The low–Pt CCL is three to four times thinner than the high–Pt CCL, hence with the same D_{ox}, R_{ox} of the low–Pt CCL would have been three times lower, than of the high–Pt CCL, as it follows from Eq.(12). Thus, Figure 8 shows that the oxygen diffusion coefficient in void pores of the low–Pt CCL is about five to six times less than in the high–Pt CCL. This is another indication that the low–Pt CCL is partially flooded.

The ratio $D_{ox}^{high}/D_{ox}^{low}$ can also be estimated from the peak frequencies. The characteristic frequency f_3^{high} in the high–Pt cell is about 200 Hz (Figure 7). Taking into account that in the low–Pt cell $f_3^{low} \simeq 450$ Hz and the ratio of CCL

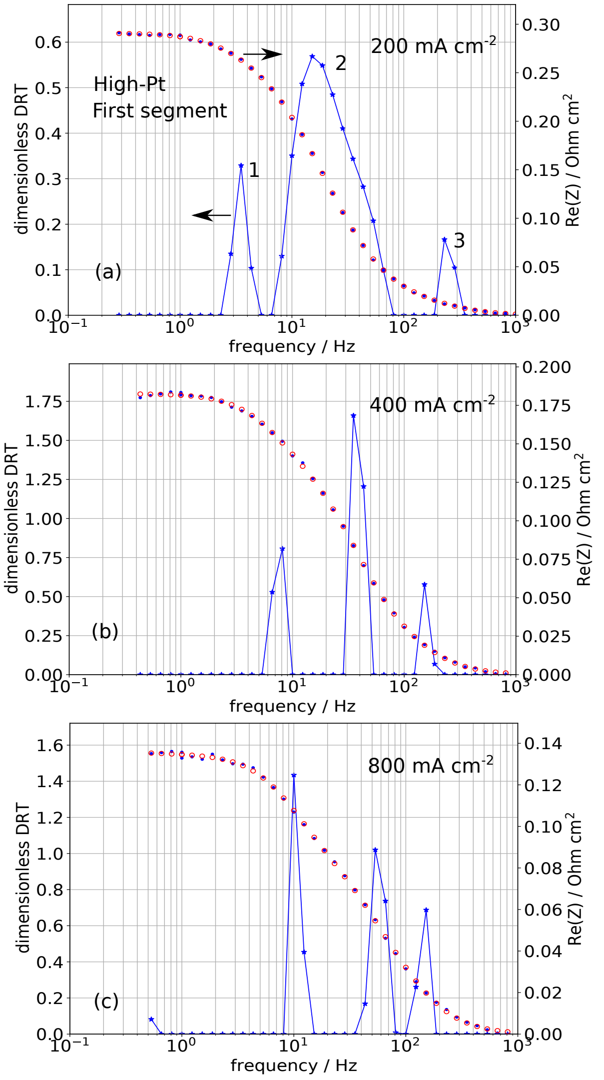

FIG. 7. DRT of the first segment in a high–Pt PEMFC. See caption to Figure 3 for curves meaning.

thicknesses in the high–Pt and low–Pt cells is about 3.5 (Table I), from Warburg finite–length formula it follows that the ratio

$$\frac{D_{ox}^{high}}{D_{ox}^{low}} = \frac{f_3^{high}}{f_3^{low}} \left(\frac{l_t^{high}}{l_t^{low}}\right)^2 \simeq 5.4 \tag{13}$$

which confirms the estimate from peak resistivities above.

It is interesting to compare the sum of potential losses calculated using DRT technique with this sum resulting from polarization curves. Figure 9 shows the polarization curves of the low– and high–Pt cells used in our experiments and the relative potential loss in the low–Pt cell. The "open circuit" points in Figure 9 represent, in fact, potential of the cells operating at the current density of about 3 mA cm^{-3} due to hydrogen crossover. The difference of cell potentials ΔV_0 at the highest point of the polarization curve is due to lower superficial exchange current density j_* in the low–Pt cell. Thus, by shifting the polarization curve of the high–Pt cell down by the value of ΔV_0 we compensate for the loss due to lower j_* in the low–Pt cell. In the absence of potential losses specific to low–Pt cell, the shifted IV curve of the high–Pt cell would overlap with the low–Pt cell curve. This, however, is not the case (Figure 9) and the difference of two curves can be attributed to the specific ionomer–film transport losses in a low–Pt cell (shaded area in Figure 9).

The accuracy of low–current part of the peak 2 curves in Figure 8 is low, and for comparison we take the point 800 mA cm^{-2}. At this current, from Figure 8 we get the potential losses in a low–Pt cell due to peak 2 and 3 of 44.4 mV

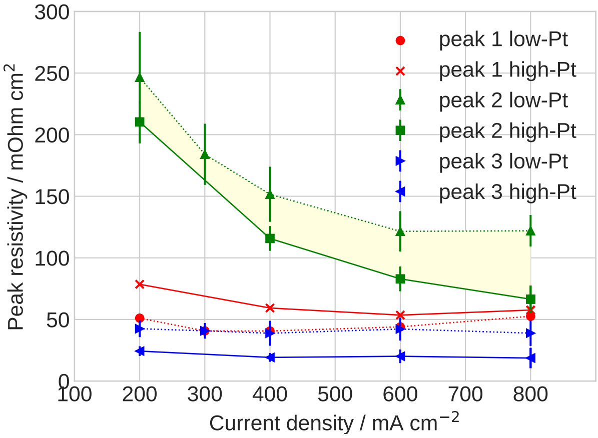

FIG. 8. Mean over ten segments polarization resistivities of peaks 1 to 3 of the low–Pt and high–Pt cells. For peak 1 the confidence intervals are not shown due to smooth variation of peak resistivity along the channel (Figure 5). Shaded area is the estimate of the ionomer film transport resistivity.

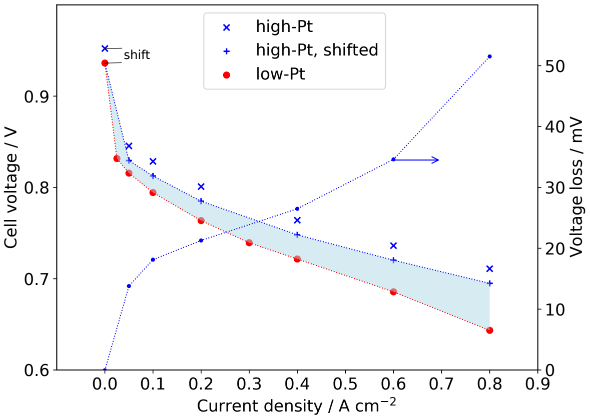

FIG. 9. Polarization curves of the high– and low–Pt cells. Crosses indicate the high–Pt curve shifted down to combine the open–circuit point with the low–Pt one. The remaining voltage losses are given by the difference of curves indicated by the crosses and large points (shaded area). The plot of the shaded area width (mV) is shown by small dots (right axis).

and 16.1 mV, respectively. The losses due to peak 1 in both the cells are almost equal and hence they do not contribute to the resulting curve. From “losses” curve in Figure 9, the total voltage loss at 800 mA cm^{-2} is $\simeq 52$ mV. Taking into account relatively large standard deviation of the third peak resistivity, the value of 52 mV agrees reasonably well with the sum of $44 + 16 = 60$ mV following from Figure 8.

It should be noted that removal of the high–frequency points with $\mathrm{Im}\,(Z) > 0$ makes it difficult determination of proton transport impedance from the DRT spectra. By the order of magnitude, the characteristic frequency f_p of proton transport in the CCl is[42]

$$f_p = \frac{2\sigma_p}{C_{dl} l_t^2} \tag{14}$$

where σ_p is the CCL proton conductivity. With the typical $C_{dl} = 20$ F cm^{-3}, $\sigma_p = 0.01$ S cm^{-1} and $l_t = 3 \cdot 10^{-4}$ cm, we get $f_p \simeq 11$ kHz. This value is well above the high–frequency cutoff of 2 kHz in our experiments. Heinzmann et al.[17] reported accurate impedance measurements up to 50 kHz and they were able to identify proton transport peaks in the DRT spectra. Unfortunately, quite high cable inductance in our setup significantly masks fuel cell impedance at the frequencies above 2–5 kHz.

IV. CONCLUSIONS

Measured local impedance spectra of a low–Pt cell with the Pt loading on the cathode side of 0.1 mg$_{Pt}$ cm^{-2} are used for calculation of distribution of relaxation times. For every cell current density in the range of 200, 300, 400, 600 and 800 mA cm^{-2} ten local spectra are acquired and processed. 48 out of 50 DRT spectra contain three peaks. Analysis shows that the leftmost peak can be attributed to oxygen transport in the gas–diffusion layer. Estimated oxygen diffusion coefficient in the GDL decreases along the air channel, indicating seemingly accumulation of liquid water in the remote segments of the GDL. Alternatively, the first peak could represent a process of oxygen transport on the GDL *and* air channel. The increase of the first peak resistivity along the channel coordinate z is then due to the growth of the low–frequency arc diameter with the distance z. To understand the nature of the middle peak, we calculated DRT of 40 local impedance spectra of the standard high–Pt cell measured for the currents of 200, 400, 600 and 800 mA cm^{-2}. Evolution of frequency and resistivity of the second peak with the cell current shows that in low–Pt cell, the second peak represents two merged processes of charge transfer and oxygen transport in ionomer film. In the high–Pt cell, the second peak represents faradaic processes only, as the role of oxygen transport in ionomer film is negligible in this cell. Thus, the difference of the second peak resistivities in the low–Pt and high–Pt cells provides an estimate of the ionomer film transport resistivity in the low–Pt cell. The third, rightmost on the frequency scale peak represents oxygen transport in void pores of the cathode catalyst layer. The third peak frequency position and resistivitiy allow us to estimate the oxygen diffusion coefficients in void pores, which shows that the void space in low–Pt cell is partially flooded.

ACKNOWLEDGMENTS

T. Reshetenko gratefully acknowledges funding from US Office of Naval Research (N00014-19-1-2159). The authors are thankful to Günter Randolf for valuable help in the system operation.

[1] Y. Ono, T. Mashio, S. Takaichi, A. Ohma, H. Kanesaka, and K. Shinohara. The analysis of performance loss with low platinum loaded cathode catalyst layers. *ECS Transactions*, 28:69–78, 2010. doi:10.1149/1.3496614.

[2] T. A. Greszler, D. Caulk, and P. Sinha. The impact of platinum loading on oxygen transport resistance. *J. Electrochem. Soc.*, 159:F831–F840, 2012. doi:10.1149/2.061212jes.

[3] J. P. Owejan, J. E. Owejan, and W. Gu. Impact of platinum loading and catalyst layer structure on PEMFC performance. *J. Electrochem. Soc.*, 160:F824–F833, 2013. doi:10.1149/2.072308jes.

[4] A. Z. Weber and A. Kusoglu. Unexplained transport resistances for low–loaded fuel–cell catalyst layers. *J. Mater. Chem. A*, 2:17207–17211, 2014. doi:10.1039/c4ta02952f.

[5] A. Kongkanand and M. F. Mathias. The priority and challenge of high-power performance of lowplatinum proton-exchange membrane fuel cells. *Phys. Chem. Lett.*, 7:1127–1137, 2016. doi:10.1021/acs.jpclett.6b00216.

[6] K. Kudo, R. Jinnouchi, and Y. Morimoto. Humidity and temperature dependences of oxygen transport resistance of nafion thin film on platinum electrode. *Electrochimica Acta*, 209:682–690, 2016. doi:10.1016/j.electacta.2016.04.023.

[7] A. T. S. Freiberg, M. C. Tucker, and A. Z. Weber. Polarization loss correction derived from hydrogen local–resistance measurement in low Pt–loaded polymer–electrolyte fuel cells. *Electrochem. Comm.*, 79:14–17, 2017. doi:10.1016/j.elecom.2017.04.008.

[8] T. Schuler, A. Chowdhury, A. T. Freiberg, B. Sneed, F. B. Spingler, M. C. Tucker, K. L. More, C. J. Radke, and A. Z. Weber. Fuel-cell catalyst-layer resistance via hydrogen limiting-current measurementss. *J. Electrochem. Soc.*, 166:F3020–F3031, 2019. doi:10.1149/2.0031907jes.

[9] H. Schichlein, A. C. Müller, M. Voigts, A. Krügel, and E. Ivers-Tiffée. Deconvolution of electrochemical impedance spectra for the identification of electrode reaction mechanisms in solid oxide fuel cells. *J. Appl. Electrochem.*, 32:875–882, 2002. doi:10.1023/A:1020599525160.

[10] A. B. Tesler, D. R. Lewin, S. Baltianski, and Y. Tsur. Analyzing results of impedance spectroscopy using novel evolutionary programming techniques. *J. Electroceram.*, 24:245–260, 2010. doi:10.1007/s10832-009-9565-z.

[11] D. Klotz, J. P. Schmidt, A. Kromp, A. Weber, and E. Ivers-Tiffée. The distribution of relaxation times as beneficial tool for equivalent circuit modeling of fuel cells and batteries. *ECS Trans.*, 41:25–33, 2012. doi:10.1149/1.3692958.

[12] Y. Zhang, Y. Chen, M. Yan, and F. Chen. Reconstruction of relaxation time distribution from linear electrochemical impedance spectroscopy. *J. Power Sources*, 283:464–477, 2015. doi:10.1016/j.jpowsour.2015.02.107.

[13] B. A. Boukamp. Derivation of a distribution function of relaxation times for the (fractal) finite length warburg. *Electrochim. Acta*, 252: 154–163, 2017. doi:10.1016/j.electacta.2017.08.154.

[14] M. Heinzmann, A. Weber, and E. Ivers-Tiffée. Impedance modelling of porous electrode structures in polymer electrolyte membrane fuel cells. *J. Power Sources*, 444:227279, 2019. doi:10.1016/j.jpowsour.2019.227279.

[15] E. Ivers-Tiffée and A. Weber. Evaluation of electrochemical impedance spectra by the distribution of relaxation times. *J. Ceramic Soc. Japan*, 125:193–201, 2017. doi:10.2109/jcersj2.16267.

[16] A. Weiss, S. Schindler, S. Galbiati, M. A. Danzer, and R. Zeis. Distribution of relaxation times analysis of high-temperature pem fuel cell impedance spectra. *Electrochim. Acta*, 230:391–398, 2017. doi:10.1016/j.electacta.2017.02.011.

[17] M. Heinzmann, A. Weber, and E. Ivers-Tiffée. Advanced impedance study of polymer electrolyte membrane single cells by means of distribution of relaxation times. *J. Power Sources*, 402:24 – 33, 2018. doi:10.1016/j.jpowsour.2018.09.004.

[18] T. Reshetenko and A. Kulikovsky. Distribution of relaxation times: A tool for measuring oxygen transport resistivity of a low–Pt PEM fuel cell cathode. *J. Electrochem. Soc.*, 167:144505, 2020. doi:10.1149/1945-7111/abc10f.

[19] M. Saccoccio, T. H. Wan, C. Chen, and Ciucci F. Optimal regularization in distribution of relaxation times applied to electrochemical impedance spectroscopy: Ridge and lasso regression methods - a theoretical and experimental study. *Electrochim. Acta*, 147:470–482, 2014. doi:10.1016/j.electacta.2014.09.058.

[20] T. H. Wan, M. Saccoccio, C. Chen, and F. Ciucci. Influence of the discretization methods on the distribution of relaxation times deconvolution: Implementing radial basis functions with DRTtools. *Electrochim. Acta*, 184:483–499, 2015. doi:10.1016/j.electacta.2015.09.097.

[21] J. Macutkevic, J. Banys, and A. Matulis. Determination of the distribution of the relaxation times from dielectric spectra. *Nonlin. Analysis: Modelling and Control*, 9:75–88, 2004. doi:10.15388/NA.2004.9.1.15172.

[22] S. Effendy, J. Song, and M. Z. Bazant. Analysis, design, and generalization of electrochemical impedance spectroscopy (EIS) inversion algorithms. *J. Electrochem. Soc.*, 167:106508, 2020. doi:10.1149/1945-7111/ab9c82.

[23] C. L. Lawson and R. J. Hanson. *Solving Least Squares Problems*. Prentice-Hall, Englewood Cliffs, NJ, USA, 1974.

[24] Andrei Kulikovsky. PEM fuel cell distribution of relaxation times: A method for calculation and behavior of oxygen transport peak. *Phys. Chem. Chem. Phys.*, 22:19131–19138, 2020. doi:10.1039/D0CP02094J.

[25] T. Reshetenko, V. Laue, U. Krewer, and K. Artyushkova. Study of degradation and spatial performance of low Pt-loaded proton exchange membrane fuel cells under exposure to sulfur dioxide in an oxidant stream. *J. Power Sources*, 458:228032, 2020. doi:10.1016/j.jpowsour.2020.228032.

[26] T. Reshetenko and B.L. Ben. Spatial performance of high- and low-Pt loaded proton exchange membrane fuel cells under cathode exposure to nitrogen dioxide. *J. Power Sources*, 458:229657, 2092. doi:10.1016/j.jpowsour.2021.229657.

[27] T. V. Reshetenko, G. Bender, K. Bethune, and R. Rocheleau. Systematic study of back pressure and anode stoichiometry effects on spatial PEMFC performance distribution. *Electrochimica Acta*, 56:8700–8710, 2011. doi:10.1016/j.electacta.2011.07.058.

[28] T. Reshetenko and A. Kulikovsky. A single–pore model for cathode catalyst layer impedance: The effect of Nafion film on PEM fuel cell performance. *RSC Adv.*, 9:38797–38806, 2019. doi:10.1039/C9RA07794D.

[29] T. M. Correia, A. P. Gibson, M. Schweiger, and J. C. Hebden. Selection of regularization parameter for optical topography. *J. Biomed. Optics*, 14:1–11, 2009. doi:10.1117/1.3156839.

[30] A. Kulikovsky. Analytical impedance of oxygen transport in a PEM fuel cell channel. *J. Electrochem. Soc.*, 166:F306–F311, 2019. doi: 10.1149/2.0951904jes.

[31] I. A. Schneider, S. A. Freunberger, D. Kramer, A. Wokaun, and G. G. Scherer. Oscillations in gas channels. Part I. The forgotten player in impedance spectroscopy in PEFCs. *J. Electrochem. Soc.*, 154:B383–B388, 2007. doi:10.1149/1.2435706.

[32] A. A. Kulikovsky. A model for local impedance of the cathode side of PEM fuel cell with segmented electrodes. *J. Electrochem. Soc.*, 159: F294–F300, 2012. doi:10.1149/2.066207jes.

[33] G. Maranzana, J. Mainka, O. Lottin, J. Dillet, A. Lamibrac, A. Thomas, and S. Didierjean. A proton exchange membrane fuel cell impedance model taking into account convection along the air channel: On the bias between the low frequency limit of the impedance and the slope of the polarization curve. *Electrochim. Acta*, 83:13–27, 2012.

[34] A. Kulikovsky and O. Shamardina. A model for PEM fuel cell impedance: Oxygen flow in the channel triggers spatial and frequency oscillations of the local impedance. *J. Electrochem. Soc.*, 162:F1068–F1077, 2015. doi:10.1149/2.0911509jes.

[35] S. Cruz-Manzo and P. Greenwood. Analytical Warburg impedance model for EIS analysis of the gas diffusion layer with oxygen depletion in the air channel of a pemfc. *J. Electrochem. Soc.*, 2021. doi:10.1149/1945-7111/ac1031.

[36] A. A. Kulikovsky and M. Eikerling. Analytical solutions for impedance of the cathode catalyst layer in PEM fuel cell: Layer parameters from impedance spectrum without fitting. *J. Electroanal. Chem.*, 691:13–17, 2013. doi:10.1016/j.jelechem.2012.12.002.

[37] T. Reshetenko and A. Kulikovsky. PEM fuel cell characterization by means of the physical model for impedance spectra. *J. Electrochem. Soc.*, 162:F627–F633, 2015. doi:10.1149/2.1141506jes.

[38] Andrei Kulikovsky. Impedance and resistivity of low–Pt cathode in a PEM fuel cell. *J. Electrochem. Soc.*, 168:044512, 2021. doi:10.1149/1945-7111/abf508.

[39] J. Shen, J. Zhou, N. G. C. Astrath, T. Navessin, Z.-S. (Simon) Liu, C. Lei, J. H. Rohling, D. Bessarabov, S. Knights, and S. Ye. Measurement of effective gas diffusion coefficients of catalyst layers of PEM fuel cells with a Loschmidt diffusion cell. *J. Power Sources*, 96:674–678, 2011.

[40] T. Muzaffar, T. Kadyk, and M. Eikerling. Tipping water balance and the Pt loading effect in polymer electrolyte fuel cells: A model–based analysis. *Sustainable Energy & Fuels*, 2:1189–1196, 2018. doi:10.1039/C8SE00026C.

[41] A. A. Kulikovsky. One–dimensional impedance of the cathode side of a PEM fuel cell: Exact analytical solution. *J. Electrochem. Soc.*, 162: F217–F222, 2015. doi:10.1149/2.0151503jes.

[42] Andrei Kulikovsky. Analysis of proton and electron transport impedance of a PEM fuel cell in H_2/N_2 regime. *Electrochem. Sci. Adv.*, e202000023, 2020. doi:10.1002/elsa.202000023.